Investigation of Ionospheric Small-Scale Plasma Structures associated with Particle Precipitation

F. Enengl[1], L. Spogli[2,5], D. Kotova[1], Y. Jin[1], K. Oksavik[3,4], N. Partamies[4], W.J. Miloch[1]

[1]Department of Physics, University of Oslo, P.O. Box 1048 Blindern, N-0316 Oslo, Norway
[2]Istituto Nazionale di Geofisica e Vulcanologia, Via di Vigna Murata 605, 00143 Rome, Italy
[3]Birkeland Centre for Space Science, Department of Physics and Technology, University of Bergen, Bergen, Norway
[4]Arctic Geophysics, University Centre in Svalbard, Longyearbyen, Norway
[5]SpacEarth Technology, Via di Vigna Murata 605, 00143 Rome, Italy

Key Points:

- Enhanced values of the GNSS-based 1-second amplitude scintillation index are observed at auroral intensity gradients.
- The IFLC is often elevated at the same time as the S4 index, confirming the diffractive nature of observed scintillation events.
- Enhanced ionospheric currents due to auroral particle precipitation contribute to structuring below the Fresnel scale.

Corresponding author: Florine Enengl, `florine.enengl@fys.uio.no`

Abstract

We investigate the role of auroral particle precipitation in small-scale (below hundreds of meters) plasma structuring in the auroral ionosphere over the Arctic. To the scope, we together analyse data recorded by an Ionospheric Scintillation Monitor Receiver (ISMR) of Global Navigation Satellite System (GNSS) signals and by an All-Sky Camera located in Longyearbyen, Svalbard (Norway). We leverage on the raw GNSS samples provided at 50 Hz by the ISMR to evaluate amplitude and phase scintillation indices at 1 s time resolution and the Ionosphere-Free Linear Combination at 20 ms time resolution. The simultaneous use of the 1 s GNSS-based scintillation indices allows identifying the scale size of the irregularities involved in plasma structuring in the range of small (up to few hundreds of meters) and medium-scale size ranges (up to few kilometers) for GNSS frequencies and observational geometry. Additionally, they allow identifying the diffractive and refractive nature of the found fluctuations on the recorded GNSS signals. Six strong auroral events and their effects on plasma structuring are studied. Plasma structuring down to scales of hundreds of meters are seen when strong gradients in auroral emissions at 557.7 nm cross the line of sight between the GNSS satellite and receiver. Local magnetic field measurements confirm small-scale structuring processes coinciding with intensification of ionospheric currents. Since 557.7 nm emissions primarily originate from the ionospheric E-region, plasma instabilities from particle precipitation at E-region altitudes are considered to be responsible for the signatures of small-scale plasma structuring highlighted in the GNSS scintillation data.

1 Introduction

Particle precipitation into the E and F-region ionosphere can cause plasma irregularities and structuring on various scales (Moen et al., 2013; Zou et al., 2013; van der Meeren et al., 2015; De Franceschi et al., 2019; Jin et al., 2016; Dahlgren et al., 2017; Fæhn Follestad et al., 2020; Urbar et al., 2022; Alfonsi et al., 2022; Enengl et al., 2023). As radio waves propagate through the ionosphere they undergo diffraction and refraction (Keskinen & Ossakow, 1983; Huba et al., 1985; Kintner & Seyler, 1985). This results in rapid fluctuations of the phase and amplitude as observed by ground-based receivers (Hey et al., 1946; Kintner et al., 2007). Irregularities below the Fresnel's scale for Global Navigation Satellite System (GNSS) frequencies and observational geometry (order of few hundreds of meters) induce diffractive effects on both the amplitude and the phase of the signals recorded at ground. In fact, those small-scale irregularities act as a new wave source for the GNSS planar waves and cause interference at the receiver level, which is the primary source of scintillation (Basu et al., 1998; Wernik et al., 2003; Kintner et al., 2007). The recent literature highlighted that the fluctuations of this kind are the only one deemed to be called "scintillation", because of the stochastic nature of the induced fluctuations (McCaffrey & Jayachandran, 2019; Ghobadi et al., 2020). Besides scintillation, fluctuations on the GNSS phase measurements are induced by irregularities covering the full ranges of scales. These fluctuations are determinstic in nature, due to the dispersive nature of the ionospheric medium, and covers the full range of the ionospheric irregularities scale sizes (McCaffrey & Jayachandran, 2019). Most of the recent research about GNSS scintillation has been dedicated to efficiently evaluate the diffractive and refractive contribution in the recorded GNSS fluctuations, especially in the high-latitude ionosphere, where the highly dynamic plasma complicates such a task(McCaffrey & Jayachandran, 2019; Ghobadi et al., 2020; Spogli et al., 2021; Wang et al., 2018, 2022; Conroy et al., 2022). In this study, we investigate the role of the particle precipitation in small-scale plasma structuring in the E and F-region ionosphere and its effects on trans-ionospheric radio wave propagation over Svalbard (Norway).

One visual signature of ionosphere-magnetosphere coupling through Birkeland currents on Earth is the aurora. Using all-sky imagers with filters for the green and red auroral emission lines gives an indication of the location and altitude of the particle precipitation energy deposition. As the geomagnetic activity grows, particle precipitation leads to brighter aurora. Auroral emissions indicate particle precipitation into the E and F-region altitudes; green (557.7 nm) emissions correspond primarily to E-region altitudes, and the red (630.0 nm) emissions to F-region altitudes. The influx of energetic particles leads to increased plasma density and enhanced conductance in the ionosphere. The ionospheric plasma is then subject to electric field effects, density irregularities and particle streams. Instabilities associated with particle precipitation are kinetic instabilities, such as the two-stream instabilities or current-driven instabilities (Kropotkin, 2016). Neutrals are also present in the E-region ionosphere, which provides conditions for the Farley-Buneman instability that arises from the difference between the electron and ion velocity, caused by collisions of the ions with neutrals (Farley Jr., 1963; Buneman, 1963; Rogister & D'Angelo, 1970; Treumann, 1997). Given the impacts of particle streams into ionospheric plasma conditions, particle precipitation is proposed to contribute to ionospheric small-scale plasma structuring (Greenwald et al., 2002).

Ionospheric plasma structuring can be indirectly observed by Ionospheric Scintillation Monitor Receivers (ISMRs). The above mentioned amplitude and phase fluctuations are usually studied through the phase (σ_Φ) and amplitude (S4) scintillation indices. As anticipated above, phase scintillations are driven by ionospheric irregularities at small wave numbers and below the first Fresnel's radius for GNSS frequencies and observational geometry. Phase scintillation below the first Fresnel radius is the result of interference between different phases and can be thought of as diffractive, while phase scintillation at small wave numbers is considered refractive and produced by fluctuations of plasma density integrated along the signal path (Kintner et al., 2007). However, the overall phase fluctuations measured at ground can be split into a refractive and diffractive contribution. The refractive part of the signal is deterministic, as it can be related to the electron density and wave frequency and can be accounted for. The diffractive part is stochastic (Kintner et al., 2007; McCaffrey & Jayachandran, 2019). Amplitude scintillations are related to diffractive effects, as the refraction impacts the wave path and power but will not cause amplitude fluctuations (McCaffrey & Jayachandran, 2019). Refraction is observed for small and large scale structures, while diffraction occurs for structures equal to or below the Fresnel's scale (Kintner et al., 2007; Zheng et al., 2022). The first order refractive contribution to GNSS phase fluctuations can be accounted for by calculating the Ionosphere-Free Linear Combination (IFLC) (Carrano et al., 2013). The IFLC is a combination of the carrier phases of two received waves at different frequencies able to account for the bulk of the refractive contribution induced by the ionosphere on the phase measurements (McCaffrey & Jayachandran, 2019). The use of the IFLC has been recently adopted to improve the phase detrending scheme adopted to evaluate the phase scintillation index. In fact, phase detrending is a delicate issue for ISMRs located in the high-latitude regions (Forte, 2005; Beach, 2006), for which the standard detrending scheme based on a 6th-order Butterworth high-pass filter with a cutoff frequency of 0.1 Hz is not effective in eliminating the bulk of the refractive contributions above the Fresnel's scale. To address this issue, the Fast Iterative Filtering technique (Cicone, 2020; Cicone & Zhou, 2021) was recently used to determine a more suitable and adaptive detrending scheme, with related cutoff frequency, to provide a phase scintillation index in which the bulk of the refractive part is eliminated (Ghobadi et al., 2020; Spogli et al., 2021). Bearing this in mind, it depends on the purpose and whether one is interested in the refractive contributions as a proxy for plasma structuring processes to decide on the choice of indices and on the related detrending scheme for GNSS phase measurements. Investigating the IFLC and scintillation indices along with the temporal and spatial evolution of particle precipitation, may improve our understanding of when/where small-scale structures are present, their role in plasma structuring processes and what their nature is.

Previous studies have already laid a pathway to understand the occurrence of ionospheric irregularities in relation to particle precipitation and their impact on trans-ionospheric radio wave propagation at high latitudes. The control of the interplanetary magnetic field (IMF) extends to small-scale irregularities of plasma density associated with the large-scale structures in the ionosphere. IMF Bz northward conditions showed moderate levels of amplitude and phase scintillation were observed with highly variable decorrelation times in a study by Basu et al. (1991). The relationship between auroral particle precipitation, electric fields and ionospheric irregularities is a result of magnetosphere-ionosphere coupling. It confirms the dependence of ionospheric plasma instablities on electric fields and precipitation-induced electron density gradients (Greenwald et al., 2002). Meso-scale electron density irregularities on the dayside auroral region are found pole-ward of the nominal cusp region (Basu et al., 1998). Irregularities on the pole-ward side of the aurora are predominantly smaller than the Fresnel scale (observed as amplitude scintillation) (Conroy et al., 2022). Plasma structuring as driven by particle precipitation is proposed to be driven at the boundaries of the auroral precipitation (such as Kelvin-Helmholtz and/or Farley-Buneman) down to E-region altitudes and to play a main role in plasma structuring on various scales Enengl et al. (2023). Pole-ward moving auroral forms can cause strong ionospheric irregularities, capable of causing more severe disturbances in the cusp ionosphere for navigation signals than polar cap patches (Oksavik et al., 2015). Loss of lock events consistently appeared consistently at edges of a auroral form named westward travelling surge in a study by Semeter et al. (2017). The authors concluded the E-region (near the oxygen emissions) was the source of the irregularities.

Moving auroral structures in the E-region occurred simultaneously with the Global Positioning System (GPS) signals showing the movement of the ionospheric regions causing diffractive fading as observed by Smith et al. (2008). Refraction and diffraction occur simultaneously during scintillation (Zheng et al., 2022). Zheng et al. (2022) observed that IFLC, S4 and phase indices showed consistent fluctuations for most scintillation events. However, they observed that IFLC and S4 did not always simultaneously correspond to scintillations, as IFLC was enhanced during the geomagnetic storm and S4 is not. They suggested that IFLC during the geomagnetic storm is caused by the increased high-frequency phase power, which is related to the enhanced density of small-scale irregularities during storm periods.

The following questions still remain open: i) how do spatial and temporal characteristics of small-scale structures relate to auroral emissions? ii) how does particle precipitation contribute to Fresnel's scale structuring? In this work, we study how small-scale plasma structuring is spatially and temporally related to particle precipitation. The effects of small-scale structuring on trans-ionospheric radio-wave propagation are used to investigate times of elevated scintillation indices and understand the plasma conditions and generation of small-scale structures. To quantify small-scale structuring processes, we use scintillation indices. For auroral precipitation, we measure auroral intensity for different emission lines.

2 Approach and Data Selection

The scintillation indices used in this study are the amplitude scintillation index (S4) and the phase scintillation index (σ_ϕ) (Fremouw et al., 1978). We further use the ionosphere-free linear combination (IFLC). The scintillation indices and IFLC are calculated starting using amplitude and phase, which in ISMRs are usually sampled at 50 to 100 Hz rate for each satellite in view. The considered ISMR is a Septentrio PolaRxS/PolaRx5s multi-frequency multi-constellation receiver (Bougard et al., 2011) operated by the Istituto Nazionale di Geofisica e Vulcanologia (INGV, Italy) and situated at Longyearbyen, Svalbard (geographic coordinates: 78.17° N, 15.99° E). The receiver is operational since January 2019 and the scintillation data provided are part of the scintillation data collection (Upper atmosphere physics and radiopropagation Working Group et al., 2020) available in the electronic Space Weather Upper atmosphere (eSWua, eswua.ingv.it) data portal. In this study, we concentrate on data from the GPS and GALILEO constellation. GPS satellites are indicated by G followed by their PRN code (e.g. G01), and GALILEO satellites by E followed by their PRN code (e.g. E01). The cut-off angle to avoid multipath effects is set to 35°. Scintillation indices and IFLC are then derived according to equations presented below (Yeh & Liu, 1982; de Paula et al., 2021; Carrano et al., 2013).

The signal intensity I is calculated using the signal amplitude A:

$$I = A^2 = I_c^2 + Q_c^2, \tag{1}$$

with I_c and Q_c being the signal intensity in-phase and quadrature components (Briggs & Parkin, 1963; Yeh & Liu, 1982; Van Dierendonck A. J.; Klobuchar J.; Hua, 1993). I is then detrended using a 6th-order high-pass Butterworth filter, with a cutoff frequency of 0.1 Hz. The amplitude scintillation index S_4 is then given by:

$$S_4 = \sqrt{\frac{\langle I^2 \rangle - \langle I \rangle^2}{\langle I \rangle^2}}. \tag{2}$$

The phase was detrended with a 6th-order high-pass Butterworth filter, with a cutoff frequency of 0.1 Hz, and the accumulated phase was calculated by $2\pi\phi_c$, with ϕ_c being the carrier phase. Subsequently, the phase scintillation index σ_ϕ is calculated by:

$$\sigma_\phi = \sqrt{\langle \phi^2 \rangle - \langle \phi \rangle^2}, \tag{3}$$

as the standard deviation of the detrended measured phase (Yeh & Liu, 1982; Kintner et al., 2007).

ISMRs traditionally have a firmware able to provide the scintillation indices in quasi real-time with a 1 minute time resolution. For the purpose of our work, we decided to consider scintillation data at a better time resolution, i.e., 1 second. Such approach has been proven to be more effective in detecting small-scale irregularities triggered by particle precipitation (Materassi & Mitchell, 2007; Wang et al., 2021), which are otherwise almost absent when considered on the standard 1-minute basis (see, e.g., the climatological pictures provided in (Spogli et al., 2009; Alfonsi et al., 2011; Moen et al., 2013; De Franceschi et al., 2019)). According to what reported in (Forte & Radicella, 2002) and in their eqn. (6) and (7), scintillation indices at 1 s allow studying spatial scales of the irregularities that are below 100 m, i.e. below the Fresnel's scale, and able account to spatial variability of particle precipitation patterns.

When a GNSS signal propagates through the ionosphere, refraction occurs. The phase delay caused by this refraction is given as the refractive index ionospheric correction term R_{corr}:

$$R_{corr} = \frac{40.3}{f_c^2} \int n_e dL, \tag{4}$$

with f being the signal carrier frequency and the electron density n_e is integrated along the raypath dL (Kashcheyev et al., 2012; Zheng et al., 2022). For propagation paths, which are the same for different carrier frequencies, the R_{corr} ratio of two carrier waves is given by

$$\frac{R_{corr1}}{R_{corr2}} = \frac{f_1^2}{f_2^2}. \tag{5}$$

Carrier phase variations L_ϕ at a constant frequency are given by

$$L_\phi = r + \lambda N - R_{corr}, \tag{6}$$

with the signal wavelength λ, integer ambiguity N, and the geometric distance r. The ionosphere-free linear combination is then calculated by:

$$IFLC = \frac{f_1^2 \phi_{L1} - f_2^2 \phi_{L2}}{f_1^2 - f_2^2} = r + \frac{f_1^2}{f_1^2 - f_2^2}\lambda N - \frac{f_2^2}{f_1^2 - f_2^2}\lambda N, \tag{7}$$

with the two carrier frequencies f_1 and f_2 and the corresponding carrier phases ϕ_{L1} and ϕ_{L2}. The ionospheric refractive index correction term R_{corr} is now removed and the IFLC is non-refractive (Cordes et al., 1986; McCaffrey & Jayachandran, 2019; Carrano et al., 2013; Zheng et al., 2022). The IFLC is then considered at the same rate of the I_c and Q_c samples, i.e., 50Hz.

In this work, the auroral emissions were captured by an all-sky camera (ASC) Keo Sentry 4ix Monochromatic Imagers from KEO Scientific, operated by the University of Oslo (Norway) situated in Longyearbyen Svalbard (geographic coordinates: 78.15° N, 16.04° E). The imager is equipped with narrow band-pass filters to monitor 557.7 nm (green) and 630.0 nm (red) auroral emissions, recording images every 15–30 seconds. The green auroral emissions are projected to an altitude of 150 km (Partamies et al., 2022; Enengl et al., 2023). The red auroral images were projected to an altitude of 250 km. Observations of the brightest aurora may be influenced by the way the camera and is operated and calibrated. These observations are nevertheless a good measure for a comparison between the auroral activity and the σ_ϕ indices.

In this article, we focus on the time period of 2019-2020 (during a solar minimum) the first season where the ISMR was operational. The availability of clear all-sky, auroral images of intense particle precipitation, and simultaneous scintillation receiver data is the first filtering stage of our data set. Subsequently, we filter for a Kp index larger than 1.3 and solar wind speeds exceeding 400 km/s, to ensure ongoing geomagnetic activity. The geomagnetic and solar wind parameters were downloaded from the NASA/GSFC's OMNI data set through OMNIWeb (King & Papitashvili, 2005). Further, all events show moderate local deflections in the horizontal magnetic field H component (over 100 nT). The H component is recorded by a magnetometer network around Svalbard operated by the Tromsø Geophysical Observatory (Tanskanen, 2009). The signature of the enhancement of the westward electrojet and the substorm current wedge in superposition with eastward electrojet enhancements is imprinted as a decrease in the H component of the magnetic field at high latitudes (Akasofu, 1965; D'Onofrio et al., 2014). Six events fulfil these criteria and are studied in detail.

3 Observations

The six strong particle precipitation events are shown in the context of scintillation indices and magnetometer data indicating structuring processes and geomagnetic conditions. Figure 1 presents the two event types we encountered: long-lasting and short-lived precipitation events (Figures 1c and 1h, respectively). The data from 24th October 2019 and 6th November 2019 show observations of increased S4 index (Figures 1a and 1f), indicating below Fresnel's scale plasma structuring. Peaks in S4 index values (shown by black arrows in Figures 1a and 1f) are recorded at: 16:18, 16:20, 16:31, 16:48 UT on 24th October 2019 and 19:00, 19:18, 19:22, 19:26, 19:44, 19:50 UT on 6th November 2019. To investigate the nature and cause of these elevated S4 observations, the IFLC, auroral intensity (I), σ_ϕ and H component are investigated. The peaks corresponding to elevated S4 indices are marked for all parameters in all panels by black arrows. The IFLC is shown in Figures 1b and 1g. Besides the elevated noise level at the beginning of both event windows, correspondence between S4 and IFLC is observed for the elevated S4 values. The IFLC indicates a diffractive contribution to scintillation. The auroral intensity at the piercing point of the satellite at the auroral emission plane is presented in Figures 1c and 1h. Here, we can observe the key difference between the two events: the 24th October 2019 event has an onset of auroral particle precipitation around 16:15 and stays above 15 kR auroral intensity for the period after 16:20 UT to 16:48 UT. The 6th November 2019 event shows multiple peaks in auroral intensity at around 19:00 UT, 19:18, 19:21, 19:25, 19:42, 19:47. All of them are happening in a close minute window of the S4 index peaks, shortly before or after. The parameter σ_ϕ is shown in Figures 1d and 1i. The σ_ϕ index is a measure of small and large-scale structuring in the ionosphere.

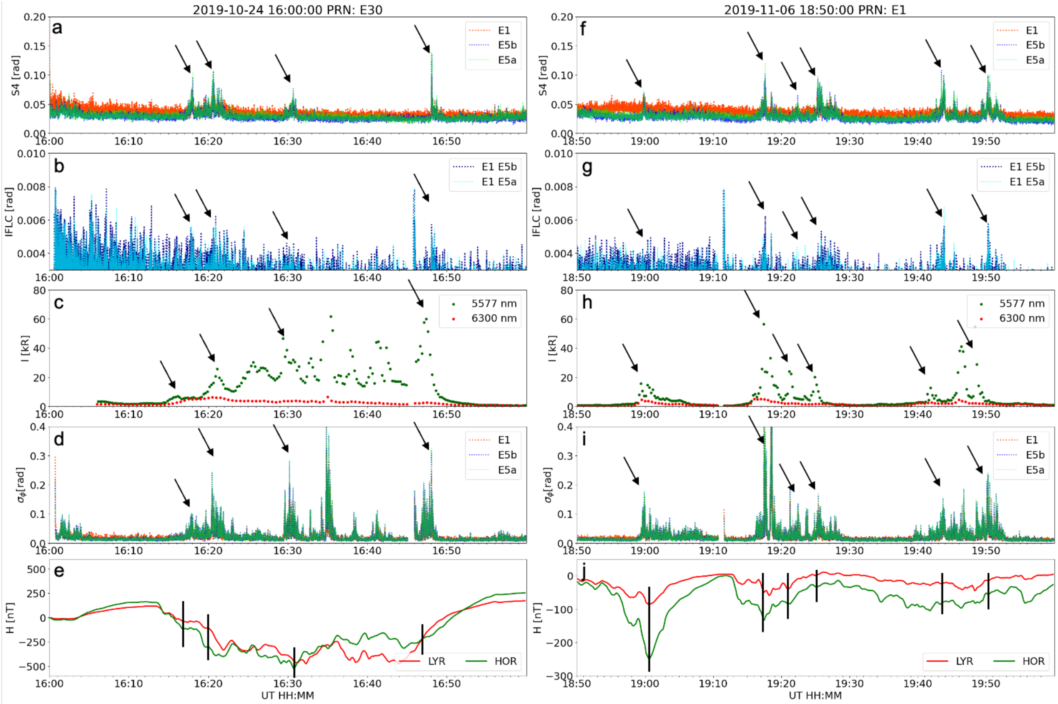

Figure 1. Small-scale plasma structures during particle precipitation. The data from 24th October 2019 and 6th November 2019 show observations of scintillation indices (S4 - panel a and f; σ_ϕ - panel d and i), the IFLC (panel b and g), magnetometer data (panel e and j), and auroral intensity (panel c and h). The peaks in S4 and IFLC mark strong intensity gradients (e.g. commence and end) of the elevated auroral intensity during strongly negative H, suggesting small-scale structuring during the commence and fading of particle precipitation. Most S4 peaks are accompanied by elevated σ_ϕ, indicating simultaneous large and small-scale structuring.

Its diffractive contribution indicating small-scales and refractive contributions all-scale ranges. The elevations in the σ_ϕ index are roughly co-located with the elevated S4 index, however not all of the σ_ϕ variations can be associated with S4 index variations, e.g. on 24th October 2019 16:35. The H component is a measure for substorm activity, shown in Figures 1e and 1j. The H component decreases at the onset of auroral particle events. We find that the changes in the H-component measured by the LYR and HOR magnetometer (see red dashed line) are mostly coinciding with the S4 variations (indicated by black vertical lines).

Additional three events are classified as long-lasting particle precipitation events as shown in the auroral intensity (Figures 2c, 2h and 2m). The events of 28th October 2019, 29th October 2019 and 7th November 2019 show the same features as the long-lasting event of 24th October 2019 in Figure 1. Comparing the S4 index shown in Figures 2a, 2f and 2k with the auroral intensity in Figures 2c, 2h and 2m shows that the elevated S4 marks the beginnings and ends of intervals of increased auroral emission intensity. This can be seen for the S4 peak at 18:28 and 19:00 UT on 28th October 2019 (2a) and in relation to the auroral intensity fading at 18:25 and 18:55 UT (Figure 2c). The IFLC (Figures 2b, 2g and 2l) and S4 index correlate for times of elevated S4 index, see e.g. 18:25, 18:35 and 18:55 UT on 28th October 2019. However, the IFLC can be noisy at times (Figure 2g at 18:30-18:45 UT on 29th October 2019). σ_ϕ variations (Figures 2d, 2i and 2n) are present for all occasions of elevated S4. The H component (Figures 2e, 2j and 2o) shows variations at aurora onset.

A second short-lived particle precipitation event is shown in Figure 3. Just as the event of 6th November 2019 shown in Figure 1, it shares the characteristics of having multiple short intense peaks in the auroral emission intensity, Figure 3 (Figure 3c), co-located with the spikes in S4 (Figure 3a). While for long-lasting events, the S4 index is elevated at intensity gradients, mainly marking the beginning and end of the auroral precipitation, for short-lasting events the precipitation can be intense and elevate the S4 index almost simultaneously. The H component (Figure 3e) repeats the pattern and shows simultaneous decreases as the auroral intensity spikes. Most S4 peaks are accompanied by elevated IFLC and σ_ϕ index.

To understand small-scale structuring in a spatial-temporal context, the piercing points of the satellites are projected onto the auroral all-sky images, see Figures 4 and 5. At two occasions the satellite PRN E30 passes through a boundary of auroral precipitation (Figures 4a and 4c) into weaker emissions/background ionosphere (Figures 4b and 4d). The auroral intensity at the piercing point of PRN E30 is peaking at 16:29:23 UT (Figure 4a) and 16:47:23 UT (Figure 4c), see also Figure 1c. The S4 index is peaking at 16:30:38 and 16:48:08 UT, see Figures 4b, 4d and Figure 1a. This happens at the same time as PRN E30 is crossing an auroral intensity gradient into weak auroral emissions (Figure 4b) / or even no auroral emissions (Figure 4d). Small-scale structures are observed at auroral intensity gradients.

Auroral particle precipitation crossing over piercing points of multiple satellites is shown in Figure 5. At 19:17:23 UT PRN G24 is outside the auroral form (Figure 5a) and shows no elevated S4 (Figure 5e). As the auroral form moves poleward, PRN G24 undergoes an intensity gradient (Figures 5b and 5c). The S4 index onsets at about 19:18 UT after passing through the intensity gradient (Figures 5d and 5e). PRN E1 is within strong auroral emissions at 19:17 UT, see Figure 5a. The S4 index is elevated latest at 19:17:38 UT (Figures 5b and 1f, and stays elevated at 19:17:53 UT (Figures 5c and 1f). However at 19:18 when PRN E1 is at the center of high auroral intensity emissions (Figure 5d), the S4 index has returned to a local minimum before the next peak. PRN E9 does not pass through any auroral emissions in the investigated time window and does not show any elevated S4 variations (Figures 5a-d and 5g). The S4 index of PRN E21 shows multiple spikes between 19:17-19:18 UT, Figures 5a-d, while it sits on a changing gradient of auroral intensity. Again, small-scale structures are observed at auroral intensity gradients.

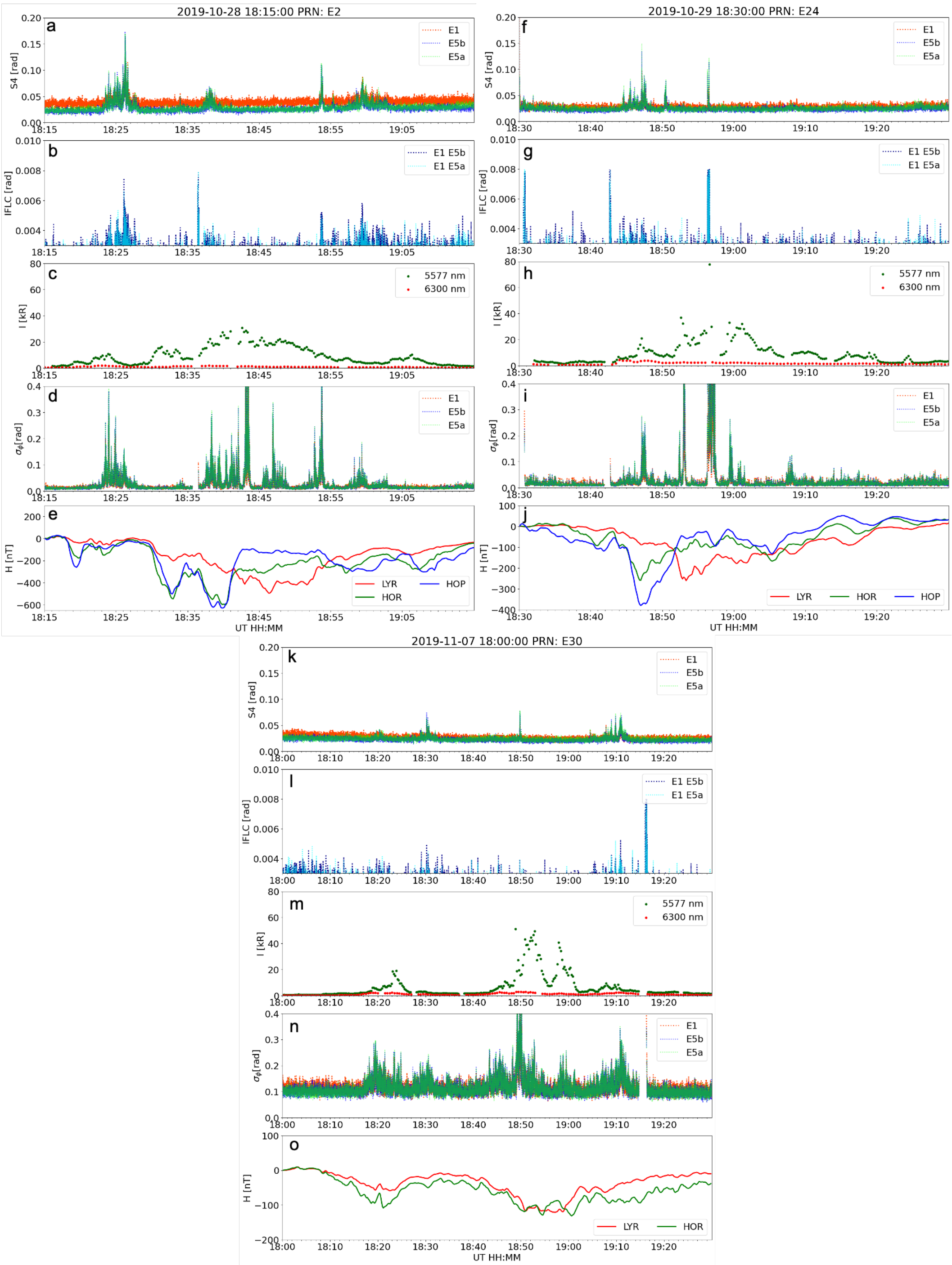

Figure 2. Small-scale plasma structures during long-lasting particle precipitation. The data from 28th October 2019, 29th October 2019 and 7th November 2019 show observations of scintillation indices (S4 - panel a, f and k; σ_ϕ - panel d, i and n), the IFLC (panel b, g, and l), magnetometer data (panel e, j and o) and auroral intensity (panel c, h and m). The peaks in S4 and IFLC mark strong intensity gradients (e.g. commence and end) of the elevated auroral intensity during strongly negative H. This suggests small-scale structuring during the commence and fading of particle precipitation. Most S4 peaks are accompanied by elevated σ_ϕ, indicating simultaneous large and small-scale structuring.

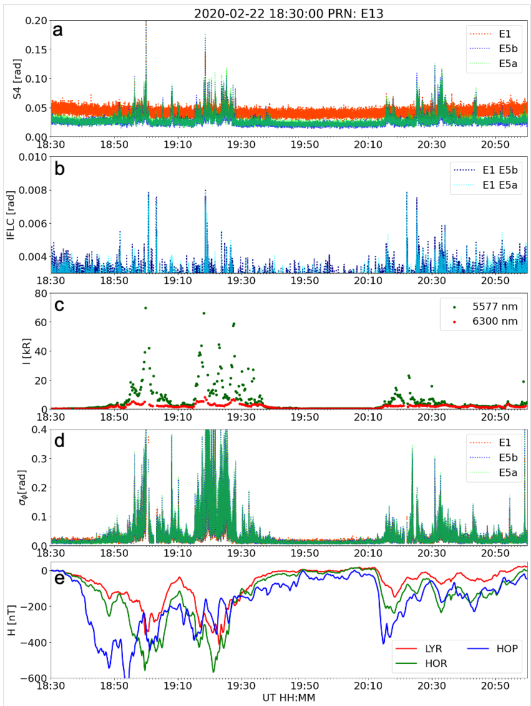

Figure 3. Small-scale plasma structures during short-lived particle precipitation event. The data from 22th February 2020 show observations of scintillation indices (S4 - panel a; σ_ϕ - panel d), the IFLC (panel b), magnetometer data (panel e) and auroral intensity (panel c). The peaks in S4 and IFLC mark strong intensity gradients of the elevated auroral intensity during strongly negative H. This suggests small-scale structuring at large intensity gradients of particle precipitation. Most S4 peaks are accompanied by elevated σ_ϕ, indicating simultaneous large and small-scale structuring.

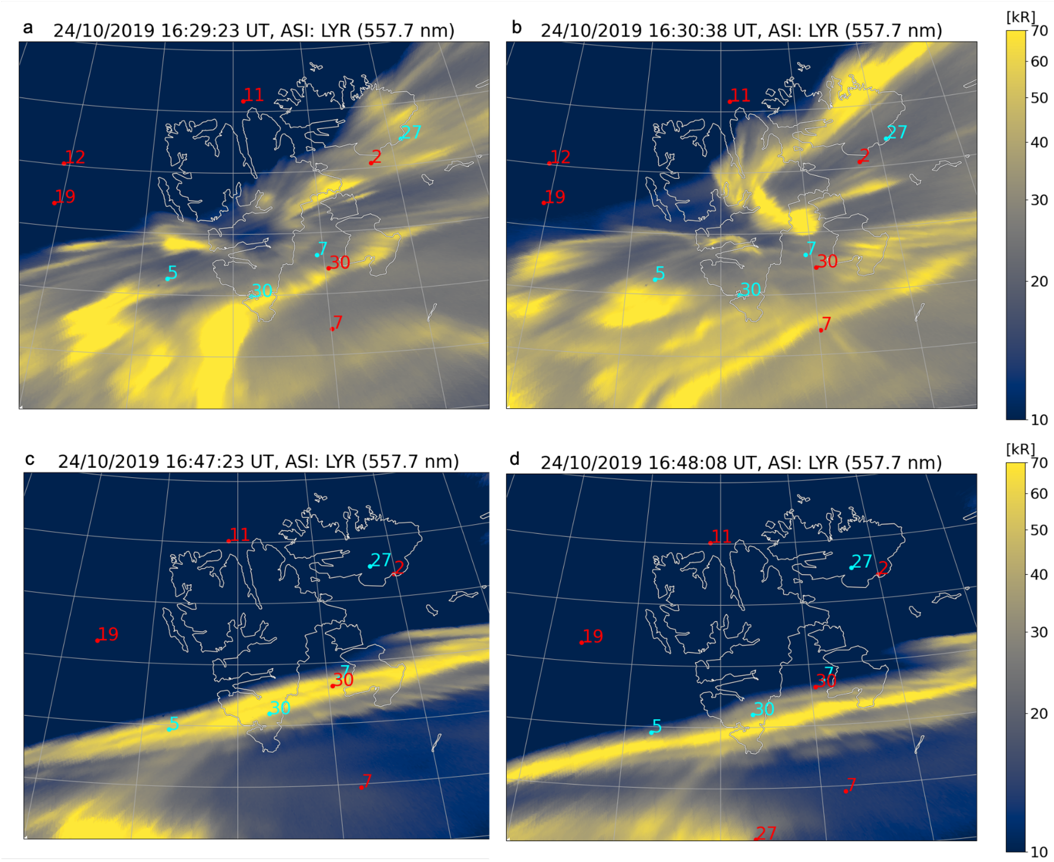

Figure 4. Spatial evolution of auroral particle precipitation and small-scale structuring at the satellite piercing point. The Figure shows all-sky images and GNSS positions relative to another projected onto 150 km altitude together with a map of Svalbard. The spatial evolution remains the same as for azimuth/elevation skyplots, as shown in the supplementary material (Figure Skyplot.png for 24th October 2019 16:30:38). Intense yellow corresponds to strong auroral intensity. GPS satellite piercing points are shown in cyan, GALILEO satellite piercing points are shown in red. Two incidents on 24th October 2019 of satellite PRN E30 passing through strong auroral emissions with a strong consequent response in increased S4 index values indicating small-scale structuring. The auroral intensity is peaking at 16:29 and 16:47 UT as shown in panels a and c. And after that, we observe elevated S4 index at 16:30 and 16:48 UT at low auroral intensity, see panels b and d. Elevated S4 indices are observed at auroral intensity gradients.

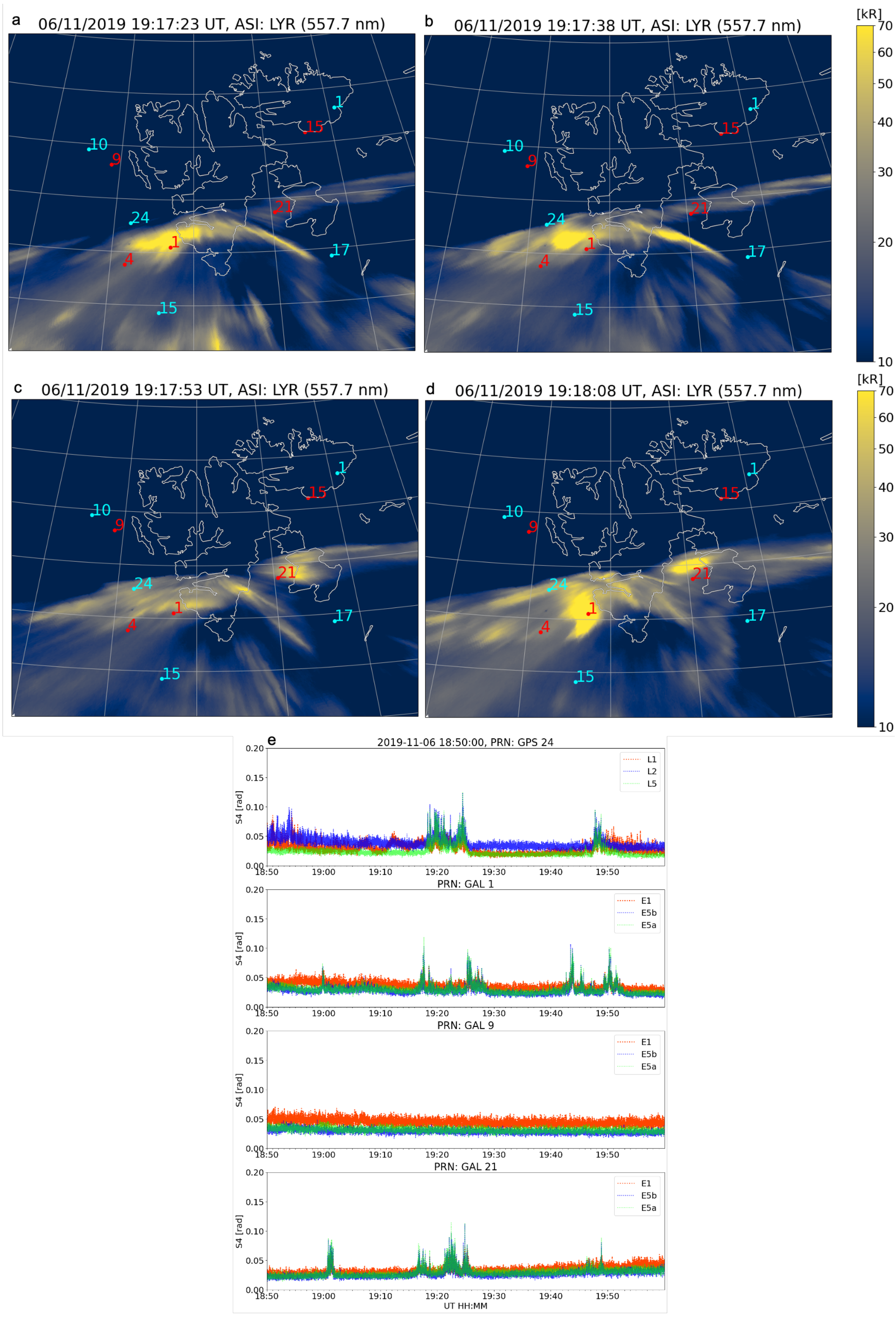

Figure 5. Auroral particle precipitation over four different satellite piercing points (PRN GPS 24, E1, E9 and E21). Panels a-d show GNSS positions and all-sky images projected to 150 km altitude together with a map of Svalbard. Intense yellow corresponds to strong auroral intensity. GPS satellite piercing points are shown in cyan, GALILEO satellite piercing points are shown in red. The S4 index variations from 18:50 to 20:00 UT are shown in panel e for the satellites PRN G24, E1, E9 and E21. Elevated S4 indices are observed for PRN G24, E1 and E21 coinciding with the particle precipitation gradient. PRN E9 does not pass through auroral precipitation and observes no small-scale plasma structuring.

4 Discussion

We have analysed the response of the amplitude scintillation index S4, evaluated on a 1 s level, to auroral particle precipitation in the evening sector 16:00–21:00 UT (MLT: 19:00–24:00) over Svalbard. Six events from the 2019/2020 season were studied with data from the LYR all-sky and LYR GNSS receiver and show intense auroral emissions (above 30 kR) and solar wind speeds exceeding 400 km/s accompanied with moderate local deflections in the H component (over 100 nT) for Kp>1.3. The events were sorted into two different types of precipitation: long-lasting (> 5 min) and short-lived (< 5 min).

In all observed events, the green auroral emissions peaked above 30 kR and were correlated with scintillation indices, whereas the red auroral emissions remained weak (below 10 kR). At times of elevated σ_ϕ and S4 values, the red auroral emissions are weak, whereas the green auroral emissions correspond to the σ_ϕ variations. This suggests that in particular E-region plasma processes and instabilities driven by auroral particle precipitation resulting in green emissions may lead to small- and large-scale plasma structuring processes that impact GNSS radio waves. In the following, we will focus on the green auroral emissions in relation to the derived scintillation indices.

For the long-lasting events, multiple peaks were observed in the S4 index indicating the beginning, end, and the intensity gradients. On 24th October 2019, the onset at 16:15 UT and fading at 16:47 UT of the particle precipitation are reflected in the S4 index increases, and so is the sharp auroral intensity increase at 16:29 UT, see again Figures 1a and 1c. The particle precipitation in the event on 28th October 2019 commences at 18:22 UT, a sharp increase in the auroral intensity is also noted at 18:36 UT and the intensity decrease is gradual after 18:53. All of these times are accompanied by S4 index increases, see again Figures 2a and 2c. The third long-lasting particle precipitation event on the 29th October 2019 shows a particle precipitation onset at 18:45 UT correlated with S4 index variations. During the event, the auroral intensity peaks around 18:57 UT and with it the S4 index, see again Figures 2f and 2h. No variations of the S4 index are found at the fading of the precipitation in this event. The event on 7th November 2019 shows an increase in the S4 index at its abrupt start at 18:50 UT, and the S4 index varies after 19:03 UT and at 19:10 UT as the intensity is fading. A shorter, just above 5-minute long event is shown at 18:20–18:30 UT with an elevated S4 index marking its beginning and end, see again Figures 2k and 2m.

The short-lived events show similar signatures of correlated precipitation and S4 index as the long-lasting events, however, as they are short the S4 index variations do not cease during the event. On the 6th November 2019, multiple peaks in the auroral intensity (19:00, 19:18, 19:22, 19:26, 19:44, 19:50 UT) are correlated to the peaks in the S4 index, see again Figures 1f and 1h. As the onset and fading happen in 1–5 minute intervals, the S4 index shows continuous variations in response. On 22nd February 2020, there were multiple short-lived auroral emission peaks that were close to one another between 19:10–19:40 UT when the satellite signal is subject to intensification of the S4 index above the noise level. The same can be observed for the other peaks (18:58, 20:30 UT) in the investigated time window, see again Figures 3a and 3c.

A correspondence between the IFLC and S4 index can be observed for most of the above listed elevated S4 index variations related to auroral particle precipitation, when there is low noise in the IFLC values (all events except 24th October 2019 at 16:00–16:20 UT), see Figures 1, 2 and 3- S4 and IFLC.

During all above listed elevated S4 index variations, we find elevated σ_ϕ values. This means that we find small-scale plasma structuring accompanied with larger scale plasma structuring. The σ_ϕ index magnitude, however, is not a measure to predict the S4 index magnitudes. Some σ_ϕ variations do not correspond to any S4 variations, such as on 24th October 2019 at 16:35 (Figure 1d) UT and 28th October 2019 at 18:40 UT (Figure 2d). The σ_ϕ index can also be elevated during long-lasting events, while the S4 index is specifically elevated at auroral intensity gradients.

Sharp decreases in the H component are found in relation to the S4 index increases. However, as the receiver to satellite line-of-sight is at a distance to the magnetometer stations, there is a delay between the observed H decreases and the S4 increases, see again Figures 1, 2 and 3 panels for the H component of the magnetic field. This indicates the ionospheric current system contributing to Fresnel's scale structuring.

Comparing the spatial evolution of the auroral emissions with the satellite piercing points and elevated S4 index (Figures 4 and 5) confirms that elevated S4 indices are found near auroral emission gradients. The highest S4 values are located at the edges of auroral forms (when moving in/out of a form) or at local intensification or weakening of auroral precipitation along the line of sight. In short, elevated S4 indices are observed at or after auroral intensity gradients along the line of sight from the satellite to the receiver.

In summary: (1) Elevated S4 values are associated with auroral intensity gradients as different levels of particle precipitation pass through the line of sight of the satellite to the receiver. (2) The IFLC often corresponds to increases of S4 index variations. (3) Intensification of ionospheric currents contributes to Fresnel-scale structuring.

In the following, we interpret the observations in terms of ionospheric plasma processes and the impacts on trans-ionospheric radio wave propagation.

During ionosphere-magnetosphere coupling, strong electric fields and currents can dissipate energy and excite plasma instabilities that create turbulence in the E-region ionosphere. The turbulence can induce nonlinear currents and strong electron heating, which can increase the global ionospheric conductance (Schlegel & St.-Maurice, 1981; Bahcivan, 2007; Dimant & Oppenheim, 2011a, 2011b). The E-region ionospheric plasma is subject to collisions with available neutrals, and energetic particle beams from the particle precipitation. Particle precipitation into the ionospheric E-region leads to a widespread irregularity dissipation and a redistribution of energy and plays a main role in E-region large-scale ionospheric plasma structuring (Makarevich et al., 2021; Enengl et al., 2023).

Both, short-lived and long-lasting particle precipitation events, show the same response of S4 index variations to precipitation, namely elevated S4 values linked to auroral intensity gradients. Auroral intensity gradients may indicate that processes at the auroral boundary, between background plasma and an energetic particle precipitation beam, contribute to small-scale plasma structuring in the E-region ionosphere. The Farley-Buneman instability (FBI) extracts its energy from the velocity difference of electrons streaming past ions, which collide with neutrals (Farley Jr., 1963; Buneman, 1963). The FBI may explain why the S4 index variations are present at the edge of strong particle precipitation gradients.

Dimant et al. (2021) states that during geomagnetic storms intense electron precipitation frequently penetrates into regions of the strong electric fields in the E-region ionosphere. Without precipitation, strong electric fields drive E-region instabilities, which further lead to plasma turbulence and increased conductance. Electron precipitation, however, dramatically raises the instability threshold, and can even largely suppress the instability inside the auroral regions. Our observations agree with Dimant et al. (2021), as we do not observe plasma structuring processes within auroral emissions, but we do observe plasma structuring at the boundaries of the particle precipitation signature.

E-region instabilities can cause electron heating, enhanced plasma particle transport and small-scale plasma turbulence that modifies large-scale ionospheric conductance and with it the entire dynamics of the near-Earth's plasma (Dimant et al., 2021). Our observations of co-located large-scale σ_ϕ index observations corresponding to small-scale amplitude index variations confirm the hypothesis of E-region dynamics affected by particle precipitation leading to large and small-scale (above and below Fresnel scale) plasma structuring.

Field-aligned currents couple the magnetosphere to the ionosphere. Particle precipitation is a signature of this phenomenon and can directly drive ionospheric plasma by structured precipitation and result in elevated scintillation index values (Boström, 1964; Carter et al., 2016; Xiong et al., 2020; Fæhn Follestad et al., 2020). In our observations, the drops in the H component confirm geomagnetic perturbations at the onset of particle precipitation and elevated scintillation indices. It suggests that the measured currents in fact contribute to FBI driving and cause plasma structuring on various scales at the auroral boundary. We can conclude that field-aligned currents not only drive large-scale plasma structuring but also below Fresnel-scale structuring, as shown by the simultaneous response of scintillation indices (σ_ϕ and S4 index variations) at the edge of field-aligned current signatures (the precipitation signatures and H component).

For the studied events, we find IFLC variations at the same time as elevated S4 index values. Zheng et al. (2022) stated that although both, IFLC and S4, are indicating diffractive variations, they however are not always correlated. This is in agreement with our fstudy, as we find IFLC correlated with S4 for most of the S4 enhancements, but not all IFLC variations are reflected in the S4 index. This may be due to high noise levels in the IFLC. The IFLC can be used as a measure for diffractive effects as the refractive part is removed. High-frequency, refractive, variations in the GPS carrier phase can be wrongly classified as scintillation, where refractive variations are deterministic and diffractive variations are stochastic (McCaffrey & Jayachandran, 2019). Care must be taken at the choice of the cutoff frequency for phase detrending or a fast iterative filtering detrending scheme can be used to provide a more realistic determination of the phase scintillation index (Ghobadi et al., 2020). We therefore carefully studied S4 and IFLC to correctly classify diffractive variations. Our results show that diffractive effects impact the signal at the onset, fading or strong changes of particle precipitation. Since σ_ϕ variations are not always found simultaneously with S4 index variations, some σ_ϕ variations can be of purely refractive nature caused by convected larger plasma structures during the particle precipitation. While at strong precipitation gradients, the σ_ϕ index also includes diffractive variations but seems otherwise to mainly include refractive signal variations. Conroy et al. (2022) suggests that high latitude phase variations are mainly of refractive nature. As the IFLC and S4 show little to no variation during long-lasting precipitation events, they are observed as refractive and deterministic. Only at the auroral intensity gradients (e.g. beginning and end) the scintillations are classified as diffractive. For short-lasting precipitation, we find IFLC and S4 elevated, therefore they are fully classified as diffractive. In summary, we observe diffractive scintillation accompanied by amplitude scintillation during strong gradients (e.g. short-lived events, beginning and ending of long-lasting events) leading to stochastic effects.

5 Conclusions

This paper investigated the response of the S4 index, evaluated from GNSS signals on a 1 second basis. to intense auroral particle precipitation events over Svalbard. The S4 index is a proxy for small-scale plasma structuring, which we find to be associated with intense particle precipitation. Elevated S4 index values can be observed under various conditions, even without strong auroral emissions. Here we specifically looked at strong auroral emissions in the evening sector during ongoing geomagnetic activity quantified by local deflections of the horizontal magnetic field component and combined with all-sky camera and scintillation receiver data at high latitudes (Longyearbyen, Svalbard). We identified 6 intense precipitation events to study the S4 response. Our results show that:

1. Clear increases in the S4 values above the noise floor level are observed at large auroral intensity gradients, as the bright aurora is moving in/out of the line of sight from the satellite to the ground receiver. The values of S4 indicate a weak scintillation activity, as S4 is never exceeding 0.2.
2. The IFLC is often elevated simultaneously with the S4 index, confirming the diffractive nature of the events.
3. Significant increases in the ionospheric currents (auroral particle precipitation) contribute to plasma structuring below the Fresnel's scale.

Why small-scale plasma structuring processes in the E-region are observed specifically at auroral intensity gradients remains an open question. Further statistical studies need to be carried out to investigate plasma instabilities like Farley-Buneman as a likely cause for small-scale structuring. Multi-instrument case studies, including in-situ measurements by rockets and satellites, are required to understand the combination of simultaneous large-scale and small-scale structuring processes driven by auroral particle precipitation, their spatial/temporal evolution and their connection with the magnetic field geometry linked to the IMF conditions.

Open Research Section

The scintillation data managed by the Istituto Nazionale di Geofisica e Vulcanologia (INGV) are available at eSWua web portal (www.eswua.ingv.it), that is operated by the Upper Atmosphere Physics and Radio propagation group of INGV.

Acknowledgments

WJM, DK and YJ acknowledge funding from the European Research Council (ERC) under the European Union's Horizon 2020 research and innovation programme (ERC Consolidator Grant agreement No. 866357, POLAR-4DSpace). This research is a part of the 4DSpace Strategic Research Initiative at the University of Oslo. KO acknowledges support from the Research Council of Norway under contract 223252. LS is grateful to Emanuele Pica and Carlo Marcocci from INGV for the support on raw GNSS data acquired by the Longyearbyen ionospheric scintillation monitor receiver. The authors are grateful to the University of Tromsø for hosting the GNSS receiver in Longyearbyen. The authors are also grateful to GRAPE (GNSS Research and Application for Polar Environment) SCAR Expert Group for supporting this study. The authors thank Bjørn Lybekk for the maintenance of the all-sky imager data.

References

Akasofu, S.-I. (1965). Dynamic morphology of auroras. *Space Science Reviews.*, *4*(4), 498. doi: https://doi.org/10.1007/BF00177092

Alfonsi, L., Bergeot, N., Cilliers, P. J., De Franceschi, G., Baddeley, L., Correia, E., ... others (2022). Review of environmental monitoring by means of radio waves in the polar regions: From atmosphere to geospace. *Surveys in Geophysics*, *43*(6), 1609–1698. doi: https://doi.org/10.1007/s10712-022-09734-z

Alfonsi, L., Spogli, L., De Franceschi, G., Romano, V., Aquino, M., Dodson, A., & Mitchell, C. N. (2011). Bipolar climatology of gps ionospheric scintillation at solar minimum. *Radio Science*, *46*(03), 1–21. doi: https://doi.org/10.1029/2010RS004571

Bahcivan, H. (2007). Plasma wave heating during extreme electric fields in the high-latitude e region. *Geophysical Research Letters*, *34*(15). doi: https://doi.org/10.1029/2006GL029236

Basu, S., Basu, S., Costa, E., Bryant, C., Valladares, C. E., & Livingston, R. C. (1991). Interplanetary magnetic field control of drifts and anisotropy of high-latitude irregularities. *Radio Science*, *26*(4), 1079-1103. doi: https://doi.org/10.1029/91RS00586

Basu, S., Weber, E. J., Bullett, T. W., Keskinen, M. J., MacKenzie, E., Doherty, P., ... Bongiolatti, J. (1998). Characteristics of plasma structuring in the cusp/cleft region at svalbard. *Radio Science*, *33*(6), 1885-1899. doi: https://doi.org/10.1029/98RS01597

Beach, T. L. (2006). Perils of the gps phase scintillation index ($\sigma\ \varphi$). *Radio Science*, *41*(5), 1–7. doi: https://doi.org/10.1029/2005RS003356

Boström, R. (1964). A model of the auroral electrojets. *Journal of Geophysical Research*, *69*(23), 4983–4999. doi: https://doi.org/10.1029/JZ069i023p04983

Bougard, B., Sleewaegen, J., Spogli, L., Veettil, S. V., & Monico, J. (2011). Cigala: Challenging the solar maximum in brazil with polarxs. In *Proceedings of the 24th international technical meeting of the satellite division of the institute of navigation (ion gnss 2011)* (pp. 2572–2579).

Briggs, B., & Parkin, I. (1963). On the variation of radio star and satellite scintillations with zenith angle. *Journal of Atmospheric and Terrestrial Physics*, *25*(6), 339-366. doi: https://doi.org/10.1016/0021-9169(63)90150-8

Buneman, O. (1963). Excitation of field aligned sound waves by electron streams. *Physical review letters*, *10*(7), 285–287. doi: https://doi.org/10.1103/PhysRevLett.10.285

Carrano, C. S., Groves, K. M., McNeil, W. J., & Doherty, P. H. (2013). Direct measurement of the residual in the ionosphere-free linear combination during scintillation. In *Proceedings of the 2013 international technical meeting of the institute of navigation* (pp. 585–596).

Carter, J. A., Milan, S. E., Coxon, J. C., Walach, M.-T., & Anderson, B. J. (2016). Average field-aligned current configuration parameterized by solar wind conditions. *Journal of Geophysical Research: Space Physics*, *121*(2), 1294-1307. doi: https://doi.org/10.1002/2015JA021567

Cicone, A. (2020). Iterative filtering as a direct method for the decomposition of nonstationary signals. *Numerical Algorithms*, *85*(3), 811–827. doi: https://doi.org/10.1007/s11075-019-00838-z

Cicone, A., & Zhou, H. (2021). Numerical analysis for iterative filtering with new efficient implementations based on fft. *Numerische Mathematik*, *147*, 1–28. doi: https://doi.org/10.1007/s00211-020-01165-5

Conroy, J. P., Deshpande, K., Scales, W., & Zaghloul, A. (2022). Statistical analysis of refractive and diffractive scintillation at high latitudes. *Radio Science*, *57*(2), e2021RS007259. doi: https://doi.org/10.1029/2021RS007259

Cordes, J. M., Pidwerbetsky, A., & Lovelace, R. V. E. (1986, November). Refractive and Diffractive Scattering in the Interstellar Medium. , *310*, 737. doi: https://doi.org/10.1086/164728

Dahlgren, H., Schlatter, N. M., Ivchenko, N., Roth, L., Karlsson, A., Dahlgren, H., ... Karlsson, A. (2017). Relation of anomalous f region radar echoes in the high-latitude ionosphere to auroral precipitation. *Annales geophysicae*, *35*(3), 475–479. doi: https://doi.org/10.5194/angeo-35-475-2017

De Franceschi, G., Spogli, L., Alfonsi, L., Romano, V., Cesaroni, C., & Hunstad, I. (2019). The ionospheric irregularities climatology over svalbard from solar cycle 23. *Scientific reports*, *9*(1), 9232. doi: https://doi.org/10.1038/s41598-019-44829-5

de Paula, E. R., Martinon, A. R. F., Moraes, A. O., Carrano, C., Neto, A. C., Doherty, P., ... Slewaegen, J. (2021). Performance of 6 different global navigation satellite system receivers at low latitude under moderate and strong scintillation. *Earth and space science (Hoboken, N.J.)*, *8*(2). doi: https://doi.org/10.1029/2020EA001314

Dimant, Y. S., Khazanov, G. V., & Oppenheim, M. M. (2021). Effects of electron precipitation on e-region instabilities: Theoretical analysis. *Journal*

of Geophysical Research: Space Physics, *126*(12), e2021JA029884. doi: https://doi.org/10.1029/2021JA029884
Dimant, Y. S., & Oppenheim, M. M. (2011a). Magnetosphere-ionosphere coupling through e region turbulence: 1. energy budget. *Journal of Geophysical Research: Space Physics*, *116*(A9). doi: https://doi.org/10.1029/2011JA016648
Dimant, Y. S., & Oppenheim, M. M. (2011b). Magnetosphere-ionosphere coupling through e region turbulence: 2. anomalous conductivities and frictional heating. *Journal of Geophysical Research: Space Physics*, *116*(A9). doi: https://doi.org/10.1029/2011JA016649
D'Onofrio, M., Partamies, N., & Tanskanen, E. (2014). Eastward electrojet enhancements during substorm activity. *Journal of Atmospheric and Solar-Terrestrial Physics*, *119*, 129-137. doi: https://doi.org/10.1016/j.jastp.2014.07.007
Enengl, F., Kotova, D., Jin, Y., Clausen, L. B., & Miloch, W. J. (2023). Ionospheric plasma structuring in relation to auroral particle precipitation. *J. Space Weather Space Clim.*, *13*, 1. doi: https://doi.org/10.1051/swsc/2022038
Farley Jr., D. T. (1963). A plasma instability resulting in field-aligned irregularities in the ionosphere. *Journal of Geophysical Research*, *68*(22), 6083-6097. doi: https://doi.org/10.1029/JZ068i022p06083
Forte, B. (2005). Optimum detrending of raw gps data for scintillation measurements at auroral latitudes. *Journal of atmospheric and solar-terrestrial physics*, *67*(12), 1100–1109. doi: https://doi.org/10.1016/j.jastp.2005.01.011
Forte, B., & Radicella, S. M. (2002). Problems in data treatment for ionospheric scintillation measurements. *Radio Science*, *37*(6), 1–5. doi: https://doi.org/10.1029/2001RS002508
Fremouw, E., Leadabrand, R., Livingston, R., Cousins, M., Rino, C., Fair, B., & Long, R. (1978). Early results from the dna wideband satellite experiment—complex-signal scintillation. *Radio Science*, *13*(1), 167–187. doi: https://doi.org/10.1029/RS013i001p00167
Fæhn Follestad, A., Herlingshaw, K., Ghadjari, H., Knudsen, D. J., McWilliams, K. A., Moen, J. I., ... Oksavik, K. (2020). Dayside field-aligned current impacts on ionospheric irregularities. *Geophysical Research Letters*, *47*(11), e2019GL086722. doi: https://doi.org/10.1029/2019GL086722
Ghobadi, H., Spogli, L., Alfonsi, L., Cesaroni, C., Cicone, A., Linty, N., ... Cafaro, M. (2020). Disentangling ionospheric refraction and diffraction effects in gnss raw phase through fast iterative filtering technique. *GPS solutions.*, *24*(3). doi: https://doi.org/10.1007/s10291-020-01001-1
Greenwald, R. A., Shepherd, S. G., Sotirelis, T. S., Ruohoniemi, J. M., & Barnes, R. J. (2002). Dawn and dusk sector comparisons of small-scale irregularities, convection, and particle precipitation in the high-latitude ionosphere. *Journal of Geophysical Research: Space Physics*, *107*(A9), SIA 1-1-SIA 1-12. doi: https://doi.org/10.1029/2001JA000158
Hey, J. S., Parsons, S. J., & Phillips, J. W. (1946). Fluctuations in cosmic radiation at radio-frequencies. *Nature (London)*, *158*(4007), 234–234. doi: https://doi.org/10.1038/158234a0
Huba, J. D., Hassam, A. B., Schwartz, I. B., & Keskinen, M. J. (1985). Ionospheric turbulence: Interchange instabilities and chaotic fluid behavior. *Geophysical research letters*, *12*(1), 65–68. doi: https://doi.org/10.1029/GL012i001p00065
Jin, Y., Moen, J. I., Miloch, W. J., Clausen, L. B. N., & Oksavik, K. (2016). Statistical study of the gnss phase scintillation associated with two types of auroral blobs. *Journal of geophysical research. Space physics*, *121*(5), 4679–4697. doi: https://doi.org/10.1002/2016JA022613
Kashcheyev, A., Nava, B., & Radicella, S. M. (2012). Estimation of higher-order ionospheric errors in gnss positioning using a realistic 3-d electron density model. *Radio Science*, *47*(4). doi: https://doi.org/10.1029/2011RS004976
Keskinen, M. J., & Ossakow, S. L. (1983). Theories of high-latitude ionospheric ir-

regularities: A review. *Radio Science*, *18*(6), 1077-1091. doi: https://doi.org/10.1029/RS018i006p01077

King, J., & Papitashvili, N. (2005). Solar wind spatial scales in and comparisons of hourly wind and ace plasma and magnetic field data. *J. Geophys. Res.*, *A02104*, 110. doi: https://doi.org/10.1029/2004JA010649

Kintner, P. M., Ledvina, B. M., & de Paula, E. R. (2007). Gps and ionospheric scintillations. *Space weather*, *5*(9), n/a. doi: https://doi.org/10.1029/2006SW000260

Kintner, P. M., & Seyler, C. E. (1985). The status of observations and theory of high latitude ionospheric and magnetospheric plasma turbulence. *Space science reviews*, *41*(1-2), 91–129. doi: https://doi.org/10.1007/BF00241347

Kropotkin, A. (2016). Formation of the small-scale structure of auroral electron precipitations. *Journal of Atmospheric and Solar-Terrestrial Physics*, *148*, 39-47. doi: https://doi.org/10.1016/j.jastp.2016.08.009

Makarevich, R. A., Crowley, G., Azeem, I., Ngwira, C., & Forsythe, V. V. (2021). Auroral e-region as a source region for ionospheric scintillation. *Journal of Geophysical Research: Space Physics*, *126*(5), e2021JA029212. doi: https://doi.org/10.1029/2021JA029212

Materassi, M., & Mitchell, C. N. (2007). Wavelet analysis of gps amplitude scintillation: A case study. *Radio Science*, *42*(01), 1–10. doi: https://doi.org/10.1029/2005RS003415

McCaffrey, A. M., & Jayachandran, P. T. (2019). Determination of the refractive contribution to gps phase "scintillation". *Journal of Geophysical Research: Space Physics*, *124*(2), 1454-1469. doi: https://doi.org/10.1029/2018JA025759

Moen, J. I., Oksavik, K., Alfonsi, L., Dåbakk, Y. R., Romano, V., & Spogli, L. (2013). Space weather challenges of the polar cap ionosphere. doi: http://doi.org/10.1051/swsc/2013025

Oksavik, K., van der Meeren, C., Lorentzen, D. A., Baddeley, L. J., & Moen, J. (2015). Scintillation and loss of signal lock from poleward moving auroral forms in the cusp ionosphere. *Journal of Geophysical Research: Space Physics*, *120*(10), 9161-9175. doi: https://doi.org/10.1002/2015JA021528

Partamies, N., Whiter, D., Kauristie, K., & Massetti, S. (2022). Magnetic local time (mlt) dependence of auroral peak emission height and morphology. *Annales Geophysicae*, *40*(5), 605–618. doi: https://doi.org/10.5194/angeo-40-605-2022

Rogister, A., & D'Angelo, N. (1970). Type ii irregularities in the equatorial electrojet. *Journal of Geophysical Research*, *75*(19), 3879–3887. doi: https://doi.org/10.1029/JA075i019p03879

Schlegel, K., & St.-Maurice, J. P. (1981). Anomalous heating of the polar e region by unstable plasma waves 1. observations. *Journal of Geophysical Research: Space Physics*, *86*(A3), 1447-1452. doi: https://doi.org/10.1029/JA086iA03p01447

Semeter, J., Mrak, S., Hirsch, M., Swoboda, J., Akbari, H., Starr, G., … Pankratius, V. (2017). Gps signal corruption by the discrete aurora: Precise measurements from the mahali experiment. *Geophysical Research Letters*, *44*(19), 9539-9546. doi: https://doi.org/10.1002/2017GL073570

Smith, A. M., Mitchell, C. N., Watson, R. J., Meggs, R. W., Kintner, P. M., Kauristie, K., & Honary, F. (2008). Gps scintillation in the high arctic associated with an auroral arc. *Space Weather*, *6*(3). doi: https://doi.org/10.1029/2007SW000349

Spogli, L., Alfonsi, L., De Franceschi, G., Romano, V., Aquino, M., & Dodson, A. (2009). Climatology of gps ionospheric scintillations over high and mid-latitude european regions. In *Annales geophysicae* (Vol. 27, pp. 3429–3437). doi: https://doi.org/10.5194/angeo-27-3429-2009

Spogli, L., Ghobadi, H., Cicone, A., Alfonsi, L., Cesaroni, C., Linty, N., ... Cafaro, M. (2021). Adaptive phase detrending for gnss scintillation detection: A case study over antarctica. *IEEE Geoscience and Remote Sensing Letters*, *19*, 1–5. doi: https://doi.org/10.1007/s10291-020-01001-1

Tanskanen, E. (2009). A comprehensive high-throughput analysis of substorms observed by image magnetometer network: Years 1993-2003 examined. *Journal of Geophysical Research*, *114, A05204*. doi: https://doi.org/10.1029/2008JA013682

Treumann, R. A. (1997). *Advanced space plasma physics.* Imperial College Press. doi: https://doi.org/10.1142/p020

Upper atmosphere physics and radiopropagation Working Group, Cesaroni, C., Marcocci, C., Pica, E., & Spogli, L. (2020). *Electronic space weather upper atmosphere database (eswua) - total electron content (tec) data, version 1.0.* Istituto Nazionale di Geofisica e Vulcanologia (INGV). Retrieved from `http://www.eswua.ingv.it/ewphp/landing.php?doi=tec` doi: 10.13127/ESWUA/TEC

Urbar, J., Spogli, L., Cicone, A., Clausen, L. B., Jin, Y., Wood, A. G., ... others (2022). Multi-scale response of the high-latitude topside ionosphere to geospace forcing. *Advances in Space Research*. doi: https://doi.org/10.1016/j.asr.2022.06.045

van der Meeren, C., Oksavik, K., Lorentzen, D. A., Rietveld, M. T., & Clausen, L. B. N. (2015). Severe and localized gnss scintillation at the poleward edge of the nightside auroral oval during intense substorm aurora. *Journal of Geophysical Research: Space Physics*. doi: https://doi.org/10.1002/2015JA021819

Van Dierendonck A. J.; Klobuchar J.; Hua, Q. (1993). Ionospheric scintillation monitoring using commercial single frequency c/a code receivers. *Proceedings of ION GPS-93*, 1333–1342.

Wang, Y., Cao, Z., Xing, Z.-Y., Zhang, Q.-H., Jayachandran, P. T., Oksavik, K., ... Shiokawa, K. (2021). Gps scintillations and tec variations in association with a polar cap arc. *Journal of Geophysical Research: Space Physics*, *126*(3), e2020JA028968. doi: https://doi.org/10.1029/2020JA028968

Wang, Y., Jayachandran, P., Ma, Y.-Z., Zhang, Q.-H., Xing, Z.-Y., Ruohoniemi, J., ... Lester, M. (2022). Dependencies of gps scintillation indices on the ionospheric plasma drift and rate of change of tec around the dawn sector of the polar ionosphere. *Journal of Geophysical Research: Space Physics*, *127*(11). doi: https://doi.org/10.1029/2022JA030870

Wang, Y., Zhang, Q.-H., Jayachandran, P., Moen, J., Xing, Z.-Y., Chadwick, R., ... Lester, M. (2018). Experimental evidence on the dependence of the standard gps phase scintillation index on the ionospheric plasma drift around noon sector of the polar ionosphere. *Journal of Geophysical Research: Space Physics*, *123*(3), 2370–2378. doi: https://doi.org/10.1002/2017JA024805

Wernik, A., Secan, J., & Fremouw, E. (2003). Ionospheric irregularities and scintillation. *Advances in Space Research*, *31*(4), 971–981. doi: https://doi.org/10.1016/S0273-1177(02)00795-0

Xiong, C., Stolle, C., Alken, P., & Rauberg, J. (2020). Relationship between large-scale ionospheric field-aligned currents and electron/ion precipitations: Dmsp observations. *Earth, Planets, and Space*, *72*(1), 1–22. doi: https://doi.org/10.1186/s40623-020-01286-z

Yeh, K. C., & Liu, C.-H. (1982). Radio wave scintillations in the ionosphere. *Proceedings of the IEEE*, *70*(4), 324–360. doi: https://doi.org/10.1109/PROC.1982.12313

Zheng, Y., Xiong, C., Jin, Y., Liu, D., Oksavik, K., Xu, C., ... Yin, F. (2022). The refractive and diffractive contributions to gps signal scintillation at high latitudes during the geomagnetic storm on 7-8 september 2017. *J. Space Weather Space Clim.*, *12*, 40. doi: 10.1051/swsc/2022036

Zou, S., Moldwin, M. B., Nicolls, M. J., Ridley, A. J., Coster, A. J., Yizengaw, E., ... Donovan, E. F. (2013). Electrodynamics of the high-latitude trough: Its relationship with convection flows and field-aligned currents. *Journal of Geophysical Research: Space Physics*, *118*(5), 2565-2572. doi: https://doi.org/10.1002/jgra.50120